Lab on a Chip

ROYAL SOCIETY OF CHEMISTRY

PAPER

View Article Online
View Journal

Cite this: DOI: 10.1039/d4lc01032a

A microfluidic platform for studying supercritical fluid crystallization and its applications†

Fatma Ercicek,[ab] Arnaud Erriguible,[ac] Olivier Nguyen,[a] Christelle Harscoat-Schiavo,[b] Pascale Subra-Paternault[b] and Samuel Marre *[a]

Received 4th December 2024,
Accepted 30th May 2025

DOI: 10.1039/d4lc01032a

rsc.li/loc

We demonstrate here the development and use of an on-chip crystallization microfluidic device combined with *in situ* analytical techniques for supercritical antisolvent crystallization. The setup facilitated real-time observation of crystallization events under pressure, giving critical insights into the time-dependent dynamics of the crystallization process. By integrating Raman spectroscopy for continuous monitoring, the system enabled precise control of local species concentrations during diffusion-driven crystallization. The microfluidic platform demonstrated effectiveness in rapid crystal screening and the identification of new co-crystals.

1. Introduction

Crystallization is a fundamental process used in various fields, including materials science and pharmaceuticals, for obtaining pure solid compounds from solutions. Traditional methods such as grinding, cooling, solvent evaporation and liquid antisolvent exhibit limitations including molecule degradation, poor reproducibility and efficiency, poor control over crystal size and morphology, and the use of large quantities of potentially harmful solvents with no direct control over the targeted crystalline phase.[1] Recent advancements have brought attention to the use of supercritical CO_2 ($scCO_2$) as an anti-solvent in crystallization processes, particularly for cocrystal formation, offering a sustainable and highly efficient alternative to conventional methodologies.[2–8]

Indeed, supercritical CO_2 displays unique properties with liquid-like density and gas-like viscosity, enabling rapid mixing and high diffusion rates, facilitating the effective crystallization of organic molecules, while allowing getting rid of any additional solvent traces in the organic crystals.[9–12] This is particularly advantageous in the pharmaceutical industry, where producing pure active pharmaceutical ingredients (APIs) is essential. The general principle of $scCO_2$-assisted crystallization involves mixing a solution containing the solute with $scCO_2$, which acts as the anti-solvent. This process reduces the solubility of the solute, creating high supersaturation and inducing nucleation. The method relies on three critical criteria: good solubility of the solute in the organic solvent, low solubility in $scCO_2$, and good miscibility between $scCO_2$ and the organic solvent.[13,14]

Nevertheless, crystallization under pressure remains a complex process, which is typically conducted in stainless steel reactors designed to withstand extreme conditions (pressure up to 20 MPa).[3,4,7,8,15,16] Understanding crystallization phenomena, such as nucleation times and kinetics, is essential for optimizing and controlling the process. Therefore, an optical access is crucial for observing and analyzing these events at the crystal scale. Here, microfluidics emerges as a promising solution to overcome these limitations.

Microfluidics and crystallization have long intersected to offer new approaches for studying and optimizing crystal formation by controlling conditions such as temperature, pH, concentration and even pressure.[17] One major advantage of microfluidics in crystallization is the ability to perform high-throughput screenings, where examples are numerous in the literature. For instance, miniaturized free interface diffusion devices can conduct hundreds of crystallization trials in parallel with volumes as small as a few nanoliters. These devices utilize molecular diffusion to mix crystallizing agents and proteins, thereby eliminating convection instabilities that could disrupt crystal growth.[18] Another approach employs droplets generated by biphasic flows, where nanoliter-sized aqueous droplets are transported in an inert oil stream.[19,20] These droplets serve as tiny crystallization reactors, allowing precise control over volume and crystallization conditions. This technique enables rapid

---

[a] Univ. Bordeaux, CNRS, Bordeaux INP, ICMCB, UMR 5026, F-33600 Pessac, France. E-mail: samuel.marre@icmcb.cnrs.fr
[b] Univ. Bordeaux, CNRS, CBMN, UMR 5248, F-33600 Pessac, France
[c] Univ. Bordeaux, CNRS, Bordeaux INP, I2M-UMR5295, F-33600 Pessac, France

† Electronic supplementary information (ESI) available. See DOI: https://doi.org/10.1039/d4lc01032a

and efficient screening of crystallization conditions with minimal protein consumption.

Besides, recent advancements in high-pressure microfluidic devices have further expanded the application of microfluidics crystallization. High-pressure microreactors, made from materials such as silicon, Pyrex[21–23] or sapphire,[24] enable precise control over temperature and pressure, facilitating *in situ* monitoring and rapid screening of crystallization processes. In addition, developments in microfluidic systems, like the μSAS (supercritical anti-solvent) process, have demonstrated significant improvements in mixing efficiency[22] and control over nucleation and growth processes.[25,26] Turbulent conditions achieved in high-pressure microfluidic devices have shown ultra-fast mixing times as small as 10^{-4}–10^{-5} seconds, highly favorable for the synthesis of organic nanoparticles.[27,28] Such advancements are increasingly important for understanding the precise mechanisms governing the size and morphology of synthesized particles, which directly impact the solubility and bioavailability of organic compounds, specifically APIs for the pharmaceutical industry. Integrating microfluidic technology with $scCO_2$-assisted crystallization effectively addresses these challenges.

Unlike previous studies on supercritical anti-solvent microfluidic processes (μSAS), which typically use turbulent conditions with co-flow geometries[25–27] and are challenging to characterize due to the ultra-fast characteristic times, our approach focuses on anti-solvent diffusion-driven crystallization at high pressure using a novel design. In contrast to rapid-mixing methods, diffusion-based systems provide slower characteristic times, enabling in-depth optical and spectroscopic *in situ* characterization. Our microfluidic platform exploits this principle by using CO_2 as an anti-solvent, which gradually diffuses into an organic phase within a confined micro-well. This method generates localized and progressive supersaturation gradients. These gradients are essential for monitoring nucleation rates and crystal growth kinetics.

This study aims to use *in situ* Raman spectroscopy for real-time monitoring of CO_2-assisted crystallization processes within high-pressure microfluidic environments. This approach aims at enhancing crystallization precision and efficiency to access real time crystal growth kinetics and to detect the appearance of new crystal phases and co-crystals by leveraging the capabilities of high-pressure microfluidic systems.

The developed microfluidic platform not only serves as a tool for crystallization but also demonstrates remarkable versatility, making it suitable for a wide range of applications. Besides its use in crystallization, the device's adaptability can easily extend to thermodynamic studies and investigations of binary and ternary systems. Its integration with *in situ* Raman spectroscopy enables real-time monitoring and precise phase identification, crucial for understanding thermodynamics and polymorphism. It can be used to provide valuable data on crystallization kinetics and mechanisms under various conditions, enhancing its utility in materials science, pharmaceuticals, and other fields where phase purity and crystallization behavior are critical.

2. Materials and methods

2.1. Chemicals

Carbon dioxide (CO_2, 99.995%) and nitrogen (N_2, 99.995%) were purchased from Messer (France). Commercially available *S*-enantiopure naproxen ((*S*)-(+)-2-(6-methoxy-2-naphthyl)propionic acid, *S*-NPX, 99%) and 4,4′-bipyridine (BiPY, 98%) were supplied by TCI Europe (Belgium) and used as received. Their respective structures are detailed in the ESI† (section 1, Fig. S1). Acetone (reagent grade, Scharlau) was acquired from Atlantic Labo (France). The *S*-NPX molecular structure was obtained from the Cambridge Structural Database (CSD), reference code COYRUD11, using the crystal structure visualization, exploration and analysis software Mercury.

2.2. Microreactor design and fabrication

A high-pressure microreactor has been designed and built with the silicon–Pyrex technology in a clean room.[21] The interest is to benefit from HP microfabrication technologies to create micro-batch reactors to confine solute solutions, which can then be exposed to $scCO_2$ for creating mixing and precipitation only driven by diffusion through a feeding micro-channel. Hence, the design consists of four crystallization circular micro-pools (Ø = 500 μm, depth = 50

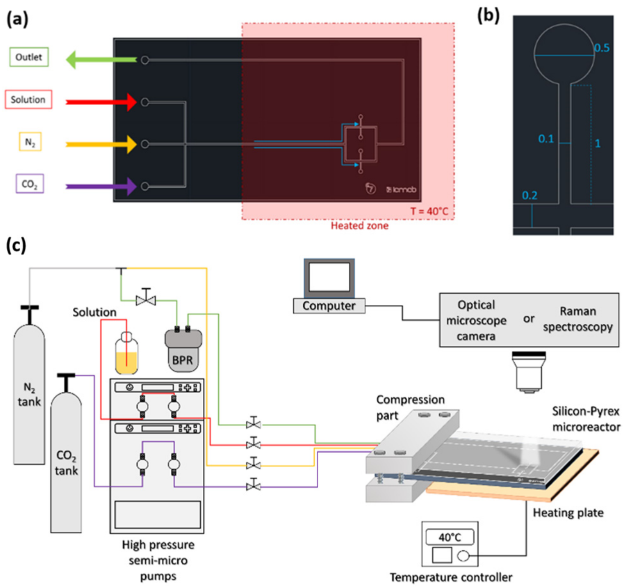

Fig. 1 (a) Pool-based design for the *in situ* on-chip crystallization experiments at 40 °C under pressure. Three inlets allow adding the API solution, N_2 and CO_2, respectively. Each inlet channel is connected to the main central channel. The blue arrows indicate the path followed by the fluid flow. (b) Enlargement of a micro-pool's design and dimensions. (c) Experimental set-up developed and used for on-chip *in situ* monitoring of API crystallization assisted by $scCO_2$.

μm) connected in pairs, in parallel with a central channel (width = 200 μm), as shown in Fig. 1. This configuration allowed $scCO_2$ to diffuse equivalently to each pool. The dimensions of the feed channels are 1 mm long and 0.1 mm wide, respectively. The geometrical parameters were chosen to ensure the absence of any convection phenomena inside the micro-pool, which was confirmed by numerical simulations realized with the open source software Notus.[28]

The silicon–Pyrex microreactor fabrication protocol was already reported elsewhere.[21] Briefly, the design pattern was designed using AutoCAD and further printed on a soft mask and was then transferred through photolithography on a silicon wafer. Then, the silicon substrate was chemically etched to reach a 50 μm microchannel depth. Next, a transparent Pyrex wafer was anodically bonded to the former wafer to seal the device, allowing optical access. An image of the finalized microreactor is shown in the ESI† (section 1, Fig. S2).

2.3. Experimental set-up and protocol

Set-up. The microreactor is linked to the external fluidic system (pump, back pressure regulator, *etc.*) by means of a compression part, previously described[21] (Fig. 1(c)). This microreactor and compression part assembly is then connected to the fluidic equipment with high-pressure fittings, tubing and valves, allowing working both in continuous or stop-flow mode. The set-up can withstand high-pressure conditions ($p < 30$ MPa), which are required for the crystallization of APIs assisted by compressed CO_2. Thanks to a heating plate, the device temperature was set at 40 °C. The microfluidic device was placed under an optical Leica microscope (Leica DM2700 M) equipped with a CCD camera (Leica DFC450) exhibiting a maximum resolution of 3072 × 2304 with a pixel pitch down to 3.4 μm and a minimum exposure time of 1 ms, using a 10× objective. A 60 mL autoclave pressurized with N_2 is used at the outlet of the system as a backpressure regulator allowing maintaining constant pressure during the experiment with a precision of ±10–3 MPa.

Protocol. The solution [*S*-NPX + solvent] is first introduced at atmospheric pressure into the microreactor heated to 40 °C using a Jasco semi-micro UHPLC pump (PU-4285) at a flowrate of 2 mL min^{-1}, taking care to flush out any air bubbles present in the micro-pools (Fig. 1(c) – red line). The entire system is then pressurized with nitrogen, an inert gas for crystallization, using the autoclave (Fig. 1(c) – green line). During this step, the solution flowrate is kept constant at 0.5 mL min^{-1}, preventing the nitrogen from replacing the solution initially introduced inside the crystallization micro-pools. The pressure is set 0.5 MPa below the desired final pressure.

Then, the excess solution in the main channel is flushed with nitrogen by slightly increasing the gas pressure (±0.3–0.5 MPa) to allow the liquid to be pushed (Fig. 1(c) – yellow line). This step is very important, as it prevents the spontaneous formation of crystals in the main channel when CO_2 is introduced.

Finally, CO_2 is injected into the main channel, replacing nitrogen (Fig. 1(c) – purple line) using a Jasco PU-4385 semi-micro CO_2 pump, to the final pressure. Considering the density of CO_2 at 8 MPa and 40 °C, and the design of the microreactor, the CO_2 flowrate was set at 0.1 mL min^{-1} for 50 seconds to ensure complete replacement of the nitrogen. Once added, the CO_2 diffuses inside the micro-pools, as depicted in the ESI† (section 1, Fig. S3), generating supersaturation, which leads to nucleation and growth of the organic crystals. The diffusion and crystallization processes are then monitored in real time with a recorded frame rate of one picture per second, allowing generating movies of the API crystal growth.

For crystallization experiments, solutions of *S*-NPX are prepared in acetone at different concentrations in the range of 20–100 mg mL^{-1} (below the saturation concentration), at room temperature. All experiments are conducted at least in duplicate.

Throughout the experiment, it is possible to distinguish the mother liquor between CO_2 and N_2 by color difference, characterizing the variation of the refractive index of the medium. Indeed, given the different surface tensions and the low miscibility of nitrogen with the naproxen *S*-NPX solution in acetone, an interface appears between these two media (Fig. 2(a)). This interface disappears with the addition of CO_2, with the mixture being supercritical. However, as the solution and CO_2 have different optical indices, it is still possible to distinguish the CO_2 flow in the solution by a light blue coloration (Fig. 2(b)).

2.4. Characterization techniques and methodology

***In situ* confocal Raman spectroscopy.** The CO_2–acetone co-diffusion process and the naproxen crystallization are monitored in real time using a confocal Raman spectrometer (HR evolution HORIBA) equipped with a CCD camera detector. The excitation laser wavelength is $\lambda = 532$ nm with a power of 10 mW. Prior to analysis, the instrument is calibrated relative to the silicon characteristic band at 520.7 cm^{-1}, using silicon from the microreactor directly. The *in situ*

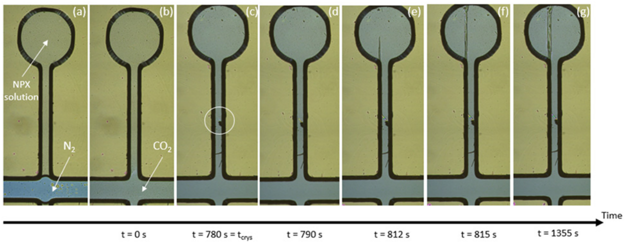

Fig. 2 Experimental images acquired during *S*-NPX precipitation with $scCO_2$ at 20 mg mL^{-1} under 8 MPa: (a) N_2 flushing, (b) CO_2 introduction, (c) first appearance of NPX crystals, (d–f) crystal growth, and (g) the final crystal habit.

measurements are performed with an exposure time of 1 s using a 10× objective and gratings with 600 lines per mm in the spectral range of 250–1900 cm^{-1}, with the UV mode when solutes are used. Repeated acquisition of the spectra in the 250–3500 cm^{-1} range with an exposure time of 30 s is performed to improve the signal-to-noise ratio for some measurements. All obtained spectra are normalized to the silicon peak of the microreactor.

Monitoring of the local CO_2–acetone composition. A calibration procedure is required to monitor the local and temporal evolution of the concentration of species confined under pressure in the microreactor.

Preliminary measurements of the {acetone + CO_2} system at thermodynamic equilibrium are carried out in the two-phase region of the mixture, at 2, 3 and 5 MPa at a temperature of 40 °C. Micro-pools are filled with acetone and the main channel with CO_2, following the protocol detailed above. Acquisitions are made every 10 minutes until equilibrium was reached. As a reminder, all spectra obtained were normalized with respect to the intensity of the silicon peak at 520.7 cm^{-1} prior to any treatment. Once equilibrium was reached, the $A_{CO_2}/A_{\text{acetone}}$ area ratios are determined. For this purpose, the A_{CO_2} area between 1260 and 1285 cm^{-1} for the CO_2 band at 1274 cm^{-1} and the A_{acetone} area between 740 and 720 cm^{-1} for the acetone band at 780 cm^{-1} are integrated. The calibration curve in the ESI† (section 1, Fig. S4) is based on the liquid phase composition of the coexisting phases at each pressure reported in the literature. The slope of this curve is further used to determine the local composition of the CO_2/acetone mixture inside the microreactor.

Numerical study of the CO_2–acetone mixing in the micro-pool. The Navier–Stokes equations and the species transport equation, assuming isothermal single-phase flow, were numerically solved using the home-made CFD code Notus,[25–28] see the ESI† (section 2). The non-ideality of the mixture was considered thanks to the Peng–Robinson equation of state. The Hayduk–Minhas coefficient for the diffusion of CO_2 in acetone has been considered.

Image analysis. The Leica Application Suite X Core (LAS X Core) and the ImageJ software are used for the images' treatment. The images taken with the optical microscope over time corresponding to a Y-mapping of the micro-pool, *i.e.* a total of 3 images, are merged and smoothed to form a unit. Roughly 170 units are obtained during a 10 min experiment. Each unit corresponds to a period of 3–5 seconds. The units are then processed on ImageJ to map the surface area of the growing crystal. The crystallization growth rate is obtained using the ready-to-use model given by Garel *et al.*[29]

3. Results and discussion

3.1. CO_2–acetone co-diffusion process

Phase equilibrium is readily attainable in short times thanks to the rapid heat and mass transfers provided by microfluidics.

To enable the observation of the crystallization process *via* a supercritical anti-solvent, we designed a custom microfluidic reactor capable of operating at high pressure and temperature (in our case up to 8 MPa & 40 °C). The device features micro-pools allowing $scCO_2$ to diffuse smoothly into the organic phase in the absence of convection. This geometry ensures a purely diffusive regime and allows direct monitoring of composition changes through *in situ* confocal Raman spectroscopy. This configuration was first tested without a solute to characterize the co-diffusion regime between acetone and $scCO_2$ prior to any crystallization attempt.

In our microreactor configuration, given the volume occupied by the solution (1.27 μL) and by the CO_2 (314.2 μL) and its density, the theoretical CO_2 molar fraction is 0.9 at 8 MPa. The CO_2–acetone vapor–liquid equilibrium (VLE) at 40 °C and the theoretical composition of CO_2 *versus* acetone in the microreactor are represented in the ESI† (section 3, Fig. S5). Under our experimental conditions (40 °C/8 MPa), the mixture remains always supercritical.

Experiments were performed in a microreactor coupled to a confocal Raman microscope for monitoring the CO_2–acetone co-diffusion at T = 40 °C and p = 8 MPa. The Raman spectrum of pure gaseous CO_2 exhibits two narrow bands corresponding to the Fermi dyad at ∼1280 cm^{-1} (ν_l) and ∼1385 cm^{-1} (ν_u)[30,31] – the exact positions of both bands depend on the density of the CO_2.[32]

Fig. 3 shows the Raman spectra taken at the center of the micro-pools, where the CO_2 Fermi dyad bands can be seen at 1275 cm^{-1} and 1375 cm^{-1} along with the characteristic acetone bands at 780 cm^{-1} (C–C stretching vibration), 1700 cm^{-1} (C=O stretching vibration), and 2920 cm^{-1} (C–H stretching vibration).[33,34] CO_2 is added at t = 0 s and several spectra are recorded over time every ∼30 s.

At t = 0 s, the acetone bands are all distinctly visible, while no band of the CO_2 Fermi doublet is present. The next acquisition, around 30 seconds later (acquisition time), already reveals a slight presence of CO_2 in the center of the micro-pool, accompanied by a modest decrease in the

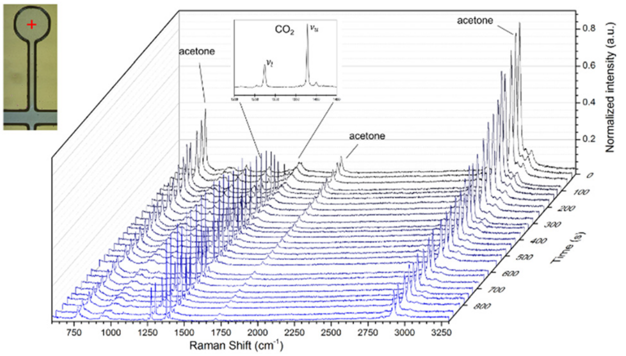

Fig. 3 Raman spectra of CO_2–acetone diffusion at the center of a micro-pool at 40 °C under 8 MPa measured at different times. All spectra were normalized to the intensity of the silicon band at 520.7 cm^{-1}.

intensity of the acetone peaks. In subsequent spectra, this decrease is very clear, indicating dilution of the acetone by the rapid arrival of CO_2. The latter assumption is supported by the appearance and, above all, the increasing intensity of the Fermi doublet peaks.

Within less than 60 seconds, the CO_2 reaches the center of the micro-pool (appearance of the CO_2 Fermi dyad bands), while the acetone bands become less intense. In about 360 seconds, the CO_2 bands hit their maximum, whereas the acetone bands lose ~60% of their intensity. Thereafter, due to mass transfer from the CO_2 to the micro-pool, the intensity of the acetone bands continues to attenuate over time, while those of the CO_2 remain stable.

A characteristic mass diffusion time in the microreactor can be estimated as: $\tau_D \sim x^2/D$, where x is the characteristic length (from the bottom of the feed channel to the center of the micro-pool: 1.025 mm) and D is the Hayduk–Minhas coefficient for the diffusion of CO_2 in acetone (2.86×10^{-8} m^2 s^{-1}) considering our operating conditions.[32,35] Given this formula, $\tau_D \sim 10$ seconds, which is in the same order as the real-time Raman monitoring.

Starting from the quantitative analysis of the recorded Raman spectra, the actual local compositions of the CO_2–acetone mixture have been calculated. Fig. 4(a) shows the evolution of the CO_2 molar fraction, as a function of time at the center of the micro-pool. At 30 seconds, the CO_2 composition in the center of the micro-pool is only $X_{CO_2} = 0.01$ under 8 MPa. After $t = 495$ seconds, the approximate time required to reach the equilibrium, the composition attained $X_{CO_2} = 0.88$. To confirm this behavior, a numerical study was performed, which is presented hereafter.

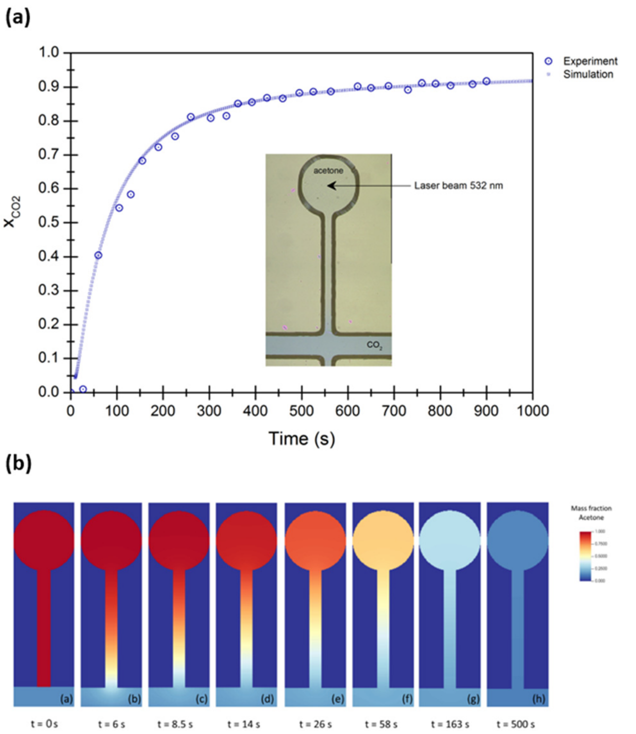

Fig. 4 (a) *In situ* quantitative analysis of the CO_2 molar fraction obtained by Raman spectrometry, which shows the CO_2–acetone co-diffusion process occurring inside the micro-pool for the pressure conditions ($p = 8$ MPa) compared to the one simulated using the CFD code Notus. (b) a–h Modelling of the CO_2–acetone composition in the micro-pool at different times for $T = 40$ °C and $p = 8$ MPa.

The images obtained from the numerical simulation are depicted in Fig. 4(b), which represents the acetone molar fraction in the CO_2–acetone mixture in the micro-pool over time for $T = 40$ °C and $p = 8$ MPa.

As seen, the acetone fraction decreases rapidly close to the initial CO_2 rich-acetone interface (Fig. 4(b)-a) and within seconds, CO_2 enters the micro-pool (Fig. 4(b)-b–e) in line with the characteristic diffusion time.

Then, at $t = 58$ seconds (Fig. 4(b)-f), the acetone mass fraction at the center of the pool corresponds to 0.68, *i.e.* to a molar fraction of 0.382 of CO_2. With increasing time, the mixture becomes richer in CO_2 (Fig. 4(b)-g at $t = 163$ s) before attaining the equilibrium (Fig. 4(b)-h) after 500 seconds. Some of the simulated values are compared to the corresponding experimental ones in Table 1.

From this comparison, it can be seen that the numerical model values are in good agreement with the experimental ones obtained by *in situ* quantitative Raman analysis, within a 1.6% error bar after 58 seconds. It is very difficult to judge the results obtained below this timeframe, due to the acquisition time required for Raman spectroscopy (30 seconds). This confirms the purely diffusive and non-convective invasion of the micro-pool by the $scCO_2$ with the considered microreactor design.

3.2. Crystallization of the *S*-NPX

Determination of the crystal detection times. In this study, the crystal detection time (t_{crys}) is defined as the elapsed time between the introduction of CO_2 into the microreactor and the visual detection of the first formed crystal *via* optical microscopy, calculated as follows:

$$t_{crys} = t_{dif} + t_{gr}$$

where t_{dif} represents the time required for $scCO_2$ to diffuse into the micro-pool, reaching a CO_2/acetone composition sufficient to generate supersaturation of the solute, and t_{gr} is the time needed for the nucleation of stable nuclei and their subsequent growth to a detectable size.

Induction time can be influenced by many factors such as agitation, temperature, and the presence of impurities,[36] as

Table 1 Modelling *vs.* experimental values of the CO_2 molar fraction in the CO_2–acetone mixture at the center of the micro-pool at $T = 40$ °C and $p = 8$ MPa

t (s)	26	58	163	500
Modelling	0.165	0.382	0.698	0.867
Experimental	0.01	0.405	0.683	0.883
Standard deviation (%)	11	1.6	1.1	1.1

well as concentration, stereoisomerism, and pressure. Therefore, *S*-NPX crystallization times were measured for p = 8 MPa and initial *S*-NPX concentration C_0 ranging from 20 to 100 mg mL^{-1}.

Effect of the initial NPX concentration. The time required for the appearance of the first naproxen crystals in the presence of $scCO_2$ was studied as a function of the initial concentration of its *S* enantiopure. The minimum detectable size with our equipment is ∽5 μm. Tests were carried out at least in duplicate.

The relationship between the induction time and the NPX concentrations at T = 40 °C and p = 8 MPa is shown in Fig. 5. A solution containing 20 mg of *S*-NPX per mL of acetone requires a latent period of 737 seconds, whereas 368 seconds is sufficient for an initial concentration of 100 mg mL^{-1} of *S*-NPX to form a detectable stable nucleus size.

A trend emerges from measurements carried out at different concentration levels. As supersaturation increases, induction time decreases, indicating that the nucleation event is significantly affected by the initial concentration of *S*-NPX. These results are expected and consistent with the classical nucleation theory.

In parallel, Raman microscopy monitoring was performed in a 40 mg mL^{-1} solution of *S*-NPX at 8 MPa, focusing on the center of the micro-well, specifically on the green dot in Fig. 6(b). The characteristic bands of *S*-NPX in solution are clearly visible at 1629 cm^{-1} (ring stretching vibration) and 1485 cm^{-1} (C–H bending)[37] in Fig. 6(a), and their intensity decreases over time along with those of acetone, as previously described for a binary mixture. However, it is not completely obvious that the *S*-NPX bands decrease as abruptly as the acetone bands, likely due to the latter's much greater intensity.

However, at t = 540 s, the recorded spectrum matches well with the one of pure CO_2 in a very dilute acetone medium (the Fermi dyad is found at 1274 and 1380 cm^{-1}); however, no traces of NPX can be seen anymore. Actually, concurrent visual inspection of the entire micro-pool reveals a single crystal of *S*-NPX that has grown next to the analyzed zone (the green dot in Fig. 6(b)). Since all the *S*-NPX molecules have been monopolized for crystal growth, the local concentration of *S*-NPX is left close to zero and can no longer be detected by Raman spectroscopy. This Raman monitoring also supports the induction time results observed optically at 40 mg mL^{-1} *S*-NPX, since microscopic observation reveals an induction time of 570 ± 30 seconds, thus, $t_{\text{crys,Raman}} \simeq t_{\text{crys,MO}}$.

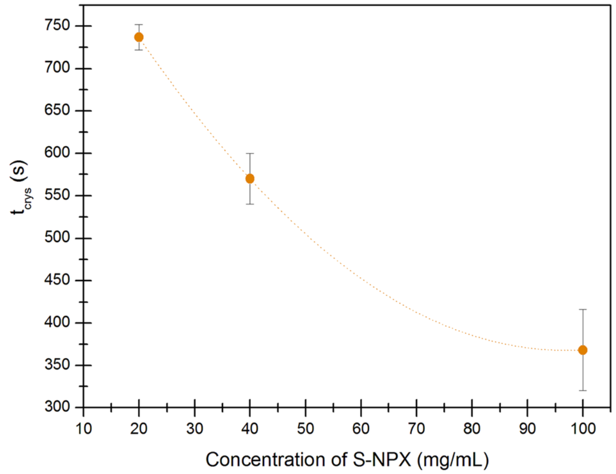

Fig. 5 Crystal detection time as a function of initial concentration of *S*-NPX (●) at T = 40 °C and p = 8 MPa. The error bars denote the standard deviation of at least two induction time points.

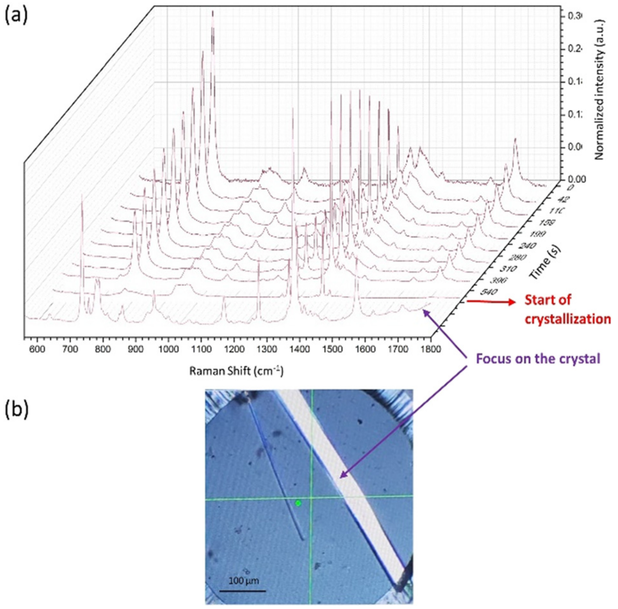

Fig. 6 (a) Raman spectra of *S*-NPX crystallization at 40 mg mL^{-1} and 8 MPa measured at different times and at the center of the micro-pool and (b) image of *S*-NPX single crystal growth.

3.3. Crystal growth monitoring

Subsequent to the formation of the first nuclei in the microreactor, naproxen crystals appear over time and their size evolution is monitored by real-time optical microscopy. In this section, the morphologies and growth of naproxen crystals obtained at different pressures and concentrations are discussed.

Morphology. *S*-NPX crystallizes as platelet- or needle-shaped single crystals around 500 μm long and 50 μm wide,

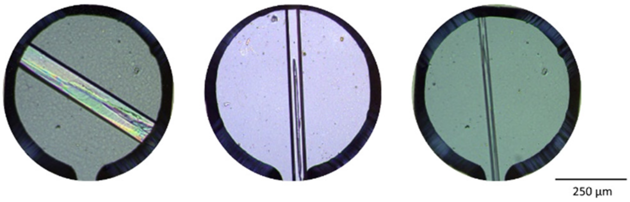

Fig. 7 Crystal habit obtained in the microreactor for *S*-NPX at 40 °C under 8 MPa at 100 mg mL^{-1} (left) and 20 mg mL^{-1} (middle and right).

irrespective of the pressure and concentration imposed during crystallization in the microreactor (Fig. 7).

This morphology is not due to a capillary-induced growth mechanism in the microreactor. It is conceivable that CO_2 diffusion in the feed microchannel directs and imposes needle-like growth. On the other hand, the crystal may grow directly inside the micro-pool, as in the first image in Fig. 7. Conversely, this is an intrinsic consequence of the homochiral structure of *S*-NPX. Enantiopure naproxen crystallizes in the space group $P2_1$ with a catemer molecular arrangement between the bonds of the –COOH acid group (Fig. 8).

Strong unidirectional hydrogen bonds in the crystal structure can lead to faster growth of organic crystals along certain crystal faces,[36,38,39] indeed, Poornachary *et al.* reported that the growth direction is the fastest along the *b*-axis for naproxen, which remains valid also during anti-solvent $scCO_2$-assisted precipitation.[39]

Crystal growth and kinetics. Growth is based on the transport of the material from the mother liquor to the crystal surface – solely by diffusion in the microreactor – followed by the incorporation of NPX molecules into a crystal lattice. Experimentally, $scCO_2$-assisted nucleation and growth of NPX crystals start mostly in the feed channel and end in the micro-pool, as shown in Fig. 2. These images correlate with the CO_2 diffusion model in acetone alone. Indeed, at the entrance to the feed channel, local supersaturation is induced by rapid CO_2 diffusion, leading to NPX nucleation and needle-like crystal growth (Fig. 2(c)). Once the first crystal has formed, a rapid decrease in solute concentration occurs in its vicinity, and crystal growth is driven by these solutes.

Thanks to microfluidics and *in situ* visualization, we were also able to estimate growth kinetics by image analysis. To do this, the crystalline surfaces of the chosen crystal were manually delimited and calculated using ImageJ for each image unit. Typically, optical microscopy images were recorded every 3 seconds, enabling crystal growth to be tracked. The crystal surfaces were then processed using the Verhulst model.[29] This application proposes a logistic regression method for estimating growth kinetics. A typical growth curve is shown in Fig. 9 for *S*-NPX at 40 mg mL^{-1} and 8 MPa. All the growth curves for other initial NPX concentrations (20, 40 and 100 mg mL^{-1}) are depicted in the ESI† (section 4, Fig. S6–S8 respectively).

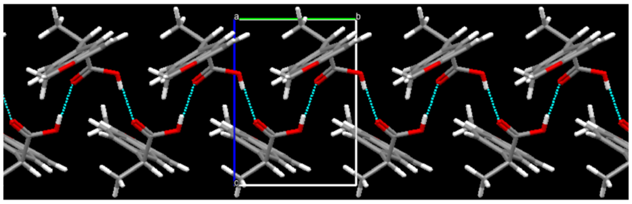

Fig. 8 Molecular arrangements of the *S*-NPX catemer structure along the *a* axis (the *b* axis is shown in green and *c* in blue), obtained with Mercury software for the reference COYRUD.

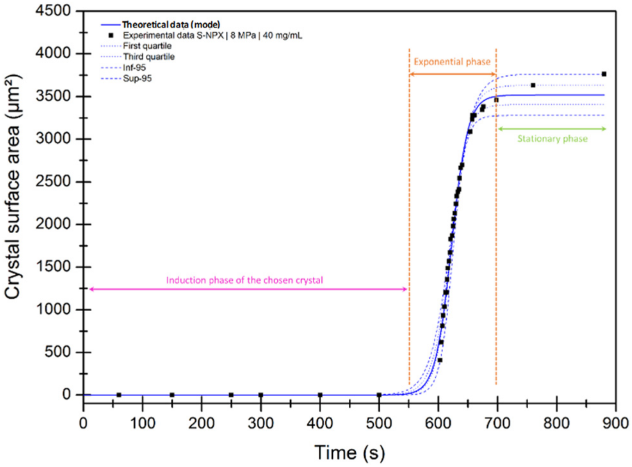

Fig. 9 Example of the logistic model (solid line) fitting the growth data (black squares) of *S*-NPX at 40 mg mL^{-1} under 8 MPa. Dotted lines - - - represent the 5 and 95% confidence intervals, while the · · · lines are the first and third quartiles.

Diffusion-controlled growth is non-linear in time and can be decomposed into three phases: the induction period, the exponential phase and the stationary phase. To estimate the growth rate, the model considers the entire growth curve. When crystal nuclei are formed and reach their critical size during the first period (with a growth rate denoted as G), they become crystals and grow rapidly at the start of the exponential phase (with a rate $G_{\max}$), while the concentration of solute near the crystal decreases sharply, forcing the crystal to reach its final morphology and characteristics (in this case, $G = 0$). The model described by Garel *et al.*[29] is based on the following equation:

$$\frac{\mathrm{d}X}{\mathrm{d}t} = G_{\max} \times X\left(1 - \frac{X}{K}\right)$$

with X being the crystal surface (2D), $G_{\max}$ the maximum growth rate and K the maximum crystal surface. The analytical solution of this equation is given by:

$$\begin{cases} X(0) = 0 \\ X(t) = \dfrac{KX_0}{X_0 + (K - X_0)\exp(-G_{\max}t)} \end{cases}$$

The growth rates of *S*-NPX crystals obtained at two distinct concentrations in the initial solution (*i.e.* 20 mg ml^{-1} and 100 mg ml^{-1}) at 8 MPa are reported in Table 2.

These differences in growth rates are consistent with previous observations. Indeed, induction times at 8 MPa, and

Table 2 *S*-NPX determined growth rates at different concentrations (20 and 100 mg mL^{-1} at p = 8 MPa, T = 40 °C)

[*S*-NPX]	8 MPa
20 mg mL^{-1}	0.575 ± 0.059 µm^2 s^{-1}
100 mg mL^{-1}	0.362 ± 0.048 µm^2 s^{-1}

especially for high concentrations, are lower, indicating a much higher nucleation rate ($t_{\mathrm{ind}} \approx 1/J$), in line with classical nucleation theory. In such cases, nucleation predominates over growth and it seems therefore natural to observe lower growth kinetics at higher concentrations.

In conclusion, *S*-NPX exhibits different kinetic behaviors when crystallized in supercritical media. Estimates of its growth kinetics at different concentrations were obtained by combining the results of image analysis and the online growth model. These data represent the first estimates of their growth kinetics in the presence of $scCO_2$ in the literature.

3.4. Co-crystal screening

These high-pressure microreactors can also be used as co-crystal screening tools. In the pharmaceutical industry, a co-crystal is defined as a solid with a single crystalline phase composed of two entities, an API and a coformer, linked *via* non-covalent interactions.[40] The strategy behind the formation of these co-crystals is to improve their physicochemical properties.[41] Usually, co-crystals are obtained by conventional crystallization techniques such as grinding or solvent evaporation.[42] Recently, CO_2-assisted co-crystallization processes have emerged as a new alternative technology. Naproxen classical co-crystallization has been studied with bipyridine (BiPY) by Manoj *et al.*,[43] and has recently been achieved with the CO_2-assisted method in our previous work.[7] Generation of co-crystals in such a microfluidic device with supercritical CO_2 has never been addressed. The microfluidic platform coupled with *in situ* Raman spectroscopy was used to rapidly confirm the production or not of naproxen and bipyridine co-crystals.

Raman tracking of a solution containing *S*-NPX and BiPY in a 2 : 1 molar ratio (known molar ratio of the co-crystal[7]), with the initial *S*-NPX concentration fixed at 40 mg mL^{-1}, at a pressure of 8 MPa is shown in Fig. 10.

CO_2 diffusion is still rapid in the micro-pool, with its characteristic Fermi dyad bands already clearly visible after only 46 seconds. As these gain in intensity, the acetone and solute bands (the bands at 1632 and 1485 cm^{-1} for *S*-NPX and 994 and 1612 cm^{-1} for BiPY) decrease until 354 seconds.

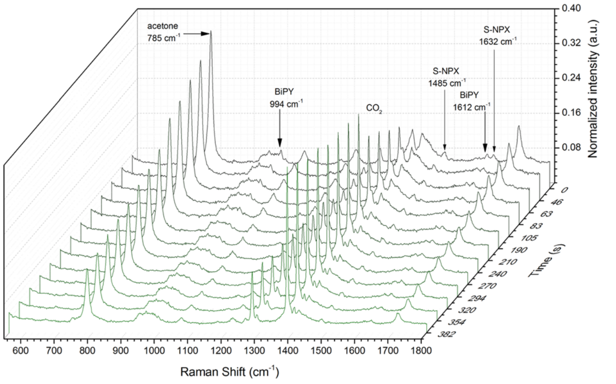

Fig. 10 Raman spectra of CO_2 diffusion in the quaternary mixture [CO_2 + acetone + *S*-NPX + BiPY] at the center of the micro-pool at 40 °C under 8 MPa measured at different times.

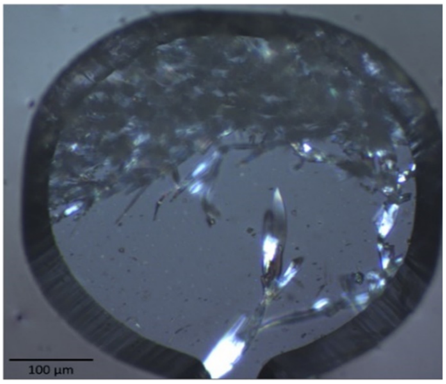

Fig. 11 Image taken after *S*-NPX and BiPY crystallization under 8 MPa at 40 °C with a confocal microscope.

Morphologically speaking, as shown in Fig. 11, the obtained crystals do not respect the homocrystalline needle-shape of *S*-NPX, assuming its effective co-crystallization with the BiPY coformer.

The Raman spectrum of the crystals produced on-chip was compared to that of the *S*-NPX : BiPY cocrystal obtained by the anti-solvent co-crystallization in a gas antisolvent (GAS) large scale reactor (see ref. 7) as shown in Fig. 12. Almost all the bands correspond perfectly to those of the co-crystal, although the intensities are higher for the co-crystal produced in GAS. It was therefore possible to create non-covalent interactions between *S*-enantiopure naproxen and bipyridine in a confined microfluidic space.

In less than 400 seconds, the $S\text{-NPX}_2 : \text{BiPY}_1$ co-crystal was generated in the microfluidic reactor. Note that the induction time of the co-crystal is shorter than that of *S*-NPX alone under the same conditions. The addition of bipyridine therefore accelerated the reaction. These results confirm

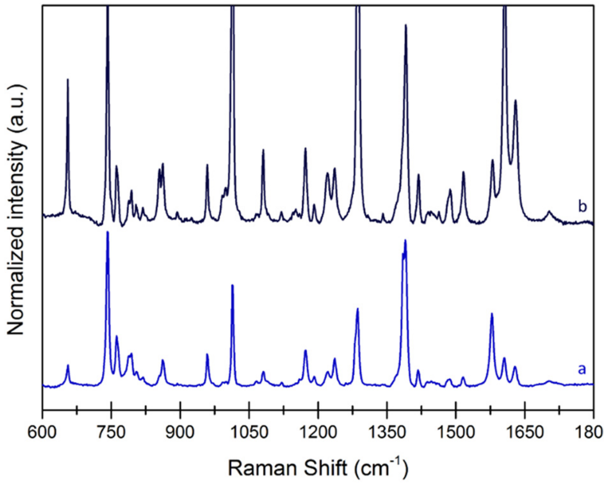

Fig. 12 Raman spectra of CO_2-processed *S*-NPX : BiPY co-crystals obtained in (a) the microreactor and (b) the GAS reactor.

those obtained from *in situ* monitoring of crystallization by infrared spectroscopy in a previous article: the presence of BiPY clearly reduces the solubility of the {*S*-NPX + BiPY} system in the CO_2–acetone mixture.

In conclusion, this microfluidic tool makes it possible to detect new co-crystalline phases in supercritical media by *in situ* Raman spectroscopy. Furthermore, solvent and reagent consumption is reduced by a factor of 6 using this strategy, compared with preparing solutions for experiments in a GAS reactor.

Conclusions

This study has successfully developed a robust and efficient design and setup for on-chip supercritical CO_2-assisted crystallization. The use of a semi-transparent microfluidic device coupled with *in situ* imaging provided valuable insights into crystallization under pressure by allowing access to time-related events. *In situ* monitoring of local species concentrations with Raman spectroscopy enabled precise control of the crystallization process. Additionally, this microfluidic platform not only proved to be effective for fast crystal screening, particularly in our case co-crystal, but it can also be used to detect polymorphism. These advancements open new opportunities in the pharmaceutical and materials science fields, offering significant potential for improving the precision and efficiency of crystallization processes, with or without pressure.

Data availability

The data supporting this article have been included as part of the ESI.†

Author contributions

F. E.: conceptualization, data curation, formal analysis, investigation, methodology, validation, visualization, writing – original draft, writing – review & editing; A. E.: conceptualization, data curation, formal analysis, software, supervision, validation, writing – review & editing; O. N.: conceptualization, methodology; C. H.-S.: funding acquisition, project administration, supervision, writing – review & editing; P. S.-P.: funding acquisition, project administration, supervision, writing – review & editing; S. M.: conceptualization, formal analysis, methodology, project administration, supervision, validation, writing – review & editing.

Conflicts of interest

There are no conflicts to declare.

Acknowledgements

The financial support of French ANR with the projects CYPRES (ANR-18-CE07-0047) and SUCRINE (ANR-22-CE51-0023) is greatly acknowledged. The authors also thank the National Research Agency, through the funding of the PEPR ORIGINS (Project: MICROFLUIDICS, ANR 22 EXOR 0013). The scientific help for Raman quantification of Max Conrad and Andreas Brauer is greatly acknowledged.

Notes and references

1 J. Chen, B. Sarma, J. M. B. Evans and A. S. Myerson, *Cryst. Growth Des.*, 2011, **11**, 887–895.
2 I. Pasquali, R. Bettini and F. Giordano, *Eur. J. Pharm. Sci.*, 2006, **27**, 299–310.
3 C. Harscoat-Schiavo, C. Neurohr, S. Lecomte, M. Marchivie and P. Subra-Paternault, *CrystEngComm*, 2015, **17**, 5410–5421.
4 C. Neurohr, A. Erriguible, S. Laugier and P. Subra-Paternault, *Chem. Eng. J.*, 2016, **303**, 238–251.
5 L. Padrela, M. A. Rodrigues, A. Duarte, A. M. A. Dias, M. E. M. Braga and H. C. de Sousa, *Adv. Drug Delivery Rev.*, 2018, **131**, 22–78.
6 L. MacEachern, A. Kermanshahi-pour and M. Mirmehrabi, *Cryst. Growth Des.*, 2020, **20**, 6226–6244.
7 F. Ercicek, C. Harscoat-Schiavo, P. Layrisse, M. Marchivie, Y. Cartigny, C. Brandel, T. Tassaing, M. Conrad, S. Marre and P. Subra-Paternault, *J. Supercrit. Fluids*, 2023, **200**, 105976.
8 F. Ercicek, M. Marchivie, L. Nimod, H. Cercel, C. Brandel, I. Ziri, Y. Cartigny, O. Monnier, S. Marre, D. Denux, P. Subra-Paternault and C. Harscoat-Schiavo, *Cryst. Growth Des.*, 2024, **24**, 4630–4644.
9 C. Pando, A. Cabanas and I. A. Cuadra, *RSC Adv.*, 2016, **6**, 71134–71150.
10 M. Knez, Z. Markocic, E. Leitgeb, M. Primozic, M. H. Knez and M. Skerget, *Energy*, 2014, **77**, 235–243.
11 N. Foster, R. Mammucari, F. Dehghani, A. Barrett, K. Bezanehtak, E. Coen, G. Combes, L. Meure, A. Ng, H. L. Regtop and A. Tandya, *Ind. Eng. Chem. Res.*, 2003, **42**, 6476–6493.
12 A. Tabernero, E. M. Martín del Valle and M. A. Galán, *Chem. Eng. Process.: Process Intesif.*, 2012, **60**, 9–25.
13 P. Subra and P. Jestin, *Powder Technol.*, 1999, **103**, 2–9.
14 P. Subra-Paternault, C. Roy, A. Vega-Gonzalez and P. Jestin, *Int. J. Chem. React. Eng.*, 2007, **5**(1), DOI: **10.2202/1542-6580.1435**.
15 P. Subra, C.-G. Laudani, A. Vega-González and E. Reverchon, *J. Supercrit. Fluids*, 2005, **35**, 95–105.
16 C. Neurohr, A.-L. Revelli, P. Billot, M. Marchivie, S. Lecomte, S. Laugier, S. Massip and P. Subra-Paternault, *J. Supercrit. Fluids*, 2013, **83**, 78–85.
17 J. Leng and J.-B. Salmon, *Lab Chip*, 2009, **9**, 24–34.
18 C. L. Hansen, E. Skordalakes, J. M. Berger and S. R. Quake, *Proc. Natl. Acad. Sci. U. S. A.*, 2002, **99**, 16531–16536.
19 B. Zheng, L. S. Roach and R. F. Ismagilov, *J. Am. Chem. Soc.*, 2003, **125**, 11170–11171.
20 B. Zheng, C. J. Gerdts and R. F. Ismagilov, *Curr. Opin. Struct. Biol.*, 2005, **15**, 548–555.
21 S. Marre, A. Adamo, S. Basak, C. Aymonier and K. F. Jensen, *Ind. Eng. Chem. Res.*, 2010, **49**, 11310–11320.

22 F. Zhang, A. Erriguible, T. Gavoille, M. T. Timko and S. Marre, *Phys. Rev. Fluids*, 2018, **3**, 092201.

23 S. Morais, N. Liu, A. Diouf, D. Bernard, C. Lecoutre, Y. Garrabos and S. Marre, *Lab Chip*, 2016, **16**, 3493–3502.

24 United States, US20230133449A1, 2023.

25 T. Jaouhari, F. Zhang, T. Tassaing, S. Fery-Forgues, C. Aymonier, S. Marre and A. Erriguible, *Chem. Eng. J.*, 2020, **397**, 125333.

26 T. Jaouhari, S. Marre, T. Tassaing, S. Fery-Forgues, C. Aymonier and A. Erriguible, *Chem. Eng. Sci.*, 2022, **248**, 117240.

27 F. Zhang, A. Erriguible and S. Marre, *Chem. Eng. Sci.*, 2019, **205**, 25–35.

28 F. Zhang, S. Marre and A. Erriguible, *Chem. Eng. J.*, 2020, **382**, 122859.

29 M. Garel, L. Izard, M. Vienne, D. Nerini, C. Tamburini and S. Martini, A ready-to-use logistic Verhulst model implemented in R shiny to estimate growth parameters of microorganisms, *bioRxiv*, 2022, preprint, DOI: 10.1101/2022.07.29.501982.

30 Y. Garrabos, V. Chandrasekharan, M. A. Echargui and F. Marsault-Herail, *Chem. Phys. Lett.*, 1989, **160**, 250–256.

31 K. M. Rosso and R. J. Bodnar, *Geochim. Cosmochim. Acta*, 1995, **59**, 3961–3975.

32 N. Liu, C. Aymonier, C. Lecoutre, Y. Garrabos and S. Marre, *Chem. Phys. Lett.*, 2012, **551**, 139–143.

33 G. Dellepiane and J. Overend, *Spectrochim. Acta*, 1966, **22**, 593–614.

34 Z. Gu, W. Chen, L. Du, H. Shi and F. Wan, *J. Appl. Spectrosc.*, 2018, **85**, 225–231.

35 T. Fadli, A. Erriguible, S. Laugier and P. Subra-Paternault, *J. Supercrit. Fluids*, 2010, **52**, 193–202.

36 J. W. Mullin, *Crystallization*, Elsevier, 2001.

37 M. O. Amin, E. Al-Hetlani and I. K. Lednev, *Sci. Rep.*, 2022, **12**, 3136.

38 P. Cheng, K. Jin, J. Cheng, F. Yang, Z. Shen, J. Chen and L. Wen, *Particuology*, 2012, **10**, 634–643.

39 S. K. Poornachary, V. D. Chia, Y. Yani, G. Han, P. S. Chow and R. B. H. Tan, *Cryst. Growth Des.*, 2017, **17**, 4844–4854.

40 F. FDA/CDER/"Stewart.

41 I. Sathisaran and S. V. Dalvi, *Pharmaceutics*, 2018, **10**(3), 108.

42 G. He, C. Jacob, L. Guo, P. S. Chow and R. B. H. Tan, *J. Phys. Chem. B*, 2008, **112**, 9890–9895.

43 K. Manoj, R. Tamura, H. Takahashi and H. Tsue, *CrystEngComm*, 2014, **16**(26), 5811–5819.